

ARTICLES

Sublattice Resolution Structural and Chemical Analysis of Individual CdSe Nanocrystals Using Atomic Number Contrast Scanning Transmission Electron Microscopy and Electron Energy Loss Spectroscopy**Andreas V. Kadavanich,^{†,‡} Tadd C. Kippeny,[‡] Meg M. Erwin,[‡] Stephen J. Pennycook,[†] and Sandra J. Rosenthal^{*,‡}***Oak Ridge National Laboratory, Solid State Division, Oak Ridge, Tennessee 37831, and Vanderbilt University, Department of Chemistry, Nashville, Tennessee 37235**Received: August 16, 2000; In Final Form: October 30, 2000*

Atomic number contrast scanning transmission electron microscopy (Z-STEM), with atomic resolution and sub-nanometer resolution scanning transmission electron microscope electron energy loss spectroscopy (STEM-EELS), was used to study single colloidal CdSe semiconductor nanocrystals embedded in MEH-PPV polymer films. The atomic column-resolved Z-STEM image provides information both on the lateral shape of the nanocrystal, as well as the relative thickness of the individual atom columns from a single image. The three-dimensional shape profile reconstructed from the data matches the predicted model. Furthermore, the sublattice is resolved so the polar surfaces can be uniquely identified. Sub-nanometer resolution EELS measurements on an individual nanocrystal indicate the presence of oxygen. The spatial distribution of the oxygen signal in the EELS measurement suggests a thin oxide layer on the nanocrystal surface.

Introduction

Colloidal semiconductor nanocrystals are an interesting basic research opportunity and offer many potential applications in biology,^{1–4} catalysis,^{5–8} and optics and electronics.^{9–15} The interest is largely due to size-dependent electronic and thermodynamic properties arising from quantum effects and the large surface-to-volume ratio. For instance, a ~ 25 Å diameter CdS nanocrystal has a band gap that is 50% (0.7 eV) larger than the bulk crystal due to quantum confinement,¹⁶ while the melting point is lowered by 1000 K due to the large surface area ($\sim 80\%$ of the atoms are at the surface).¹⁷

A common problem in the study of nanocrystals is polydispersity. With a few exceptions^{18,19} real nanocrystal samples are characterized by a distribution of sizes and shapes. While modern synthetic techniques have resulted in samples with less than 5% standard deviation on the average size,²⁰ this still implies that bulk characterization techniques provide only an average picture of nanocrystal specimens. Consequently, techniques that can characterize individual nanocrystals are of great importance. A variety of electrical^{15,21,22} and optical^{23–28} measurements have yielded insights into the physical properties of single nanocrystals. Theoretical interpretation of such results requires that the nanocrystal structure be known accurately.

In general, the theoretical description of nanocrystals has advanced to the level where detailed information on the surface structure is necessary for adequately reproducing the physical properties of nanocrystals. This is particularly true for dealing

with electronic trap states which are presumed to be associated with the nanocrystal surface.^{29–31}

At present, transmission electron microscopy (TEM) is the predominant technique for obtaining atomically resolved structural information on individual nanocrystals. However, due to the difficulty of tilting a nanocrystal specimen through a large angle, such measurements generally only yield a 2-dimensional picture of the nanocrystal structure. Three-dimensional models are then built up from analyzing different nanocrystals observed in different orientations.^{32,33} Three-dimensional information and sublattice structure is accessible from phase-contrast HRTEM, but generally requires multiple images (e.g., through-focal series)—with the increased potential for beam damage—and extensive computer processing.^{34–37}

Z-contrast STEM overcomes the limitations of HRTEM, providing three-dimensional structure together with sublattice information from a single image. Z-STEM uses an incoherent imaging process which results in images that are intuitively interpretable in terms of specimen structure and composition.^{38,39} In this paper we demonstrate that, for typical nanocrystal samples, Z-STEM can provide information on the relative thickness of different parts of a nanocrystal as well as information on the polarity of the lattice (and hence the location of polar surfaces on the nanocrystal). Additionally, the high brightness and energy stability of the Field Emission Gun (FEG) electron source in our STEM is ideally suited to high-resolution EELS analysis, which can provide elemental information on an atomic scale even for disordered regions. In particular, it allows one to analyze the chemical nature of surface adsorbates, such as the ligands or surface oxide. Indeed the two techniques are largely complementary as Z-STEM works best for the heavy

[†] Oak Ridge National Laboratory.

[‡] Vanderbilt University.

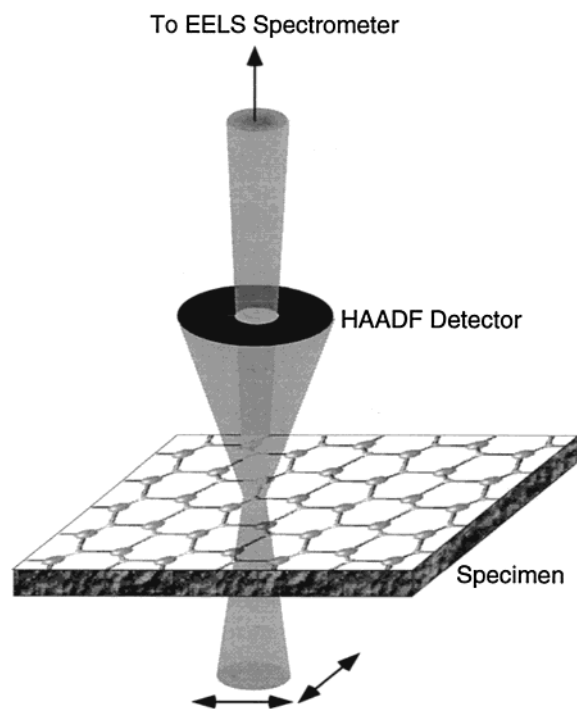


Figure 1. STEM Operation. The highly focused beam (minimum diameter 1.3 Å fwhm) enters the specimen from below and is scanned across it to form an image. The electrons are scattered off the atoms in the specimen and the HAADF detector intercepts electrons scattered at large angles. Small angle scattering passes through the HAADF detector and can be used to form a bright-field image or fed into an EELS spectrometer for analysis.

elements in the crystalline core whereas EELS is ideal for the lighter elements at the surface.

Theory

Z-Contrast STEM. Scanning transmission electron microscopy works by scanning a highly focused electron probe across a specimen and collecting all electrons scattered within a specific angular range. Like other scanning probe microscopies, spatial resolution is governed by the interaction volume of the probe electron beam interrogating the specimen rather than the resolution of the detection system. In addition, secondary signals (secondary electrons, X-rays, visible light, etc.) can be used for imaging if suitable detectors are available.

Z-STEM employs a high angle annular dark field (HAADF) detector to collect electrons scattered at a large angle (typically tens of milliradians) from the beam direction while averaging over all scattering directions perpendicular to the beam. As long as the detector covers a large angular range, the imaging process is incoherent,^{39–41} such that Z-STEM images are a direct projection of the specimen object function. Z-STEM operation is indicated schematically in Figure 1.

Unlike phase-contrast high resolution transmission electron microscope (HRTEM) images, no contrast reversals occur in Z-STEM, therefore images are intuitively interpretable in terms of the specimen's structure. Indeed, it is possible to detect individual atoms using Z-Contrast.⁴² For a detailed description of Z-Contrast see Nellist and Pennycook.^{38,39}

For a single atom, elastic incoherent scattering is described by the Rutherford scattering formula:

$$\frac{d\sigma(\theta)}{d\Omega} = \frac{e^4 Z^2}{16(E_0)^2 \sin^4 \frac{\theta}{2}} \quad (1)$$

In eq 1,³⁴ the left side of the equation denotes the differential scattering cross section as a function of the scattering angle θ . E_0 is the incident beam energy, e is the electron charge, and Z is the atomic number of the scattering nucleus.

This predicts that the beam intensity scattered into a particular angular range from the beam direction is proportional to the square of the atomic number (Z^2). For a fixed detector angle, variations in the detected intensity then arise from different atoms, with contrast proportional to Z^2 .

For crystalline specimens, this has to be modified to account for interference effects between electrons scattered from different atoms. For a thin crystalline specimens in a channeling orientation, the scattering detected at high angles is predominantly from 1s Bloch states of the fast electrons in the crystal. These states are highly localized with virtually no overlap between adjacent columns. Each column can therefore be considered as contributing independently to the image intensity.^{39–41}

Within a column, interference effects give rise to thickness-dependent contrast. Transverse vibrational motion of the atoms reduces this effect to a thickness dependent modulation of the incoherent scattering intensity. The intensity of this thermal diffuse scattering is given by the incoherent object function in eq 2, reproduced from Pennycook and Nellist.³⁹

$$O_{\text{TDS}}(\mathbf{R}, t) = \frac{Z^2 \epsilon^{\text{av}^2}}{(\xi^2 \mu^{1s^2} + \pi^2)} \left[\pi^2 (1 - e^{-2\mu^{1s} t}) - \xi^2 \mu^{1s^2} e^{-2\mu^{1s} t} \left(1 - \cos \frac{2\pi t}{\xi} - \pi \xi \mu^{1s} e^{-2\mu^{1s} t} \sin \frac{2\pi t}{\xi} \right) \right] \quad (2)$$

In eq 2,³⁹ O_{TDS} = incoherent object function due to thermal diffuse scattering from the 1s Bloch state as a function of \mathbf{R} , where \mathbf{R} = position of an atomic column perpendicular to the beam direction (a vector in the image plane) and t = column thickness. Z = atomic number, ϵ^{av} = average excitation of the 1s Bloch state, μ^{1s} = absorption coefficient for the 1s state, and ξ = extinction distance. The vibrational motion enters through the dependence of the extinction distance on the Debye–Waller factor for electron scattering.

For CdSe nanocrystals the relevant thickness range is the region below 100 Å. Values for the Cd and Se columns of wurtzite CdSe in [100] zone axis orientation are plotted in Figure 2 as a function of thickness. Also plotted is the average of the two, which is proportional to the intensity observed if the atomic columns are not resolved (or if they are summed together in the analysis). As can be seen, the object functions for both Cd and Se are increasing monotonically in this region. Hence, incoherent imaging conditions persist and the relative intensities of columns of equal composition in a Z-STEM image immediately reveal their relative thicknesses.

Furthermore, it is apparent from the plot that for equal thickness, Cd has more intensity than Se over the entire thickness range considered, although the values are considerably different from the simple Z^2 value of 1.99, which is expected in the limit of high thickness. Thus, if the atomic columns can be resolved, it is possible to distinguish between the two sublattices, which then allows one to assign unique crystallographic labels to lattice vectors and surfaces. This is particularly relevant for a polar lattice, where crystallographically similar surfaces have distinctly different chemical properties. Of specific interest for wurtzite CdSe nanocrystals is the ability to distinguish the (001) and (00 $\bar{1}$) surfaces.

EELS. While Z-STEM imaging is dominated by elastically scattered electrons, a significant fraction of the forward scattered electron intensity is due to inelastic processes in which energy

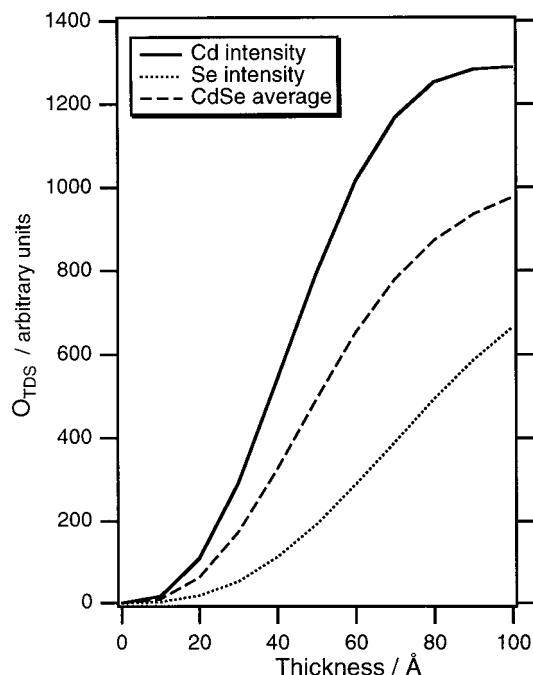


Figure 2. Thickness dependence of Z-STEM. The value of the Incoherent Object Function from eq 2 plotted against thickness for the Cd and Se columns seen in [100] zone axis projection. Also shown is the average of the two as would be observed if the atomic columns were not resolved. (Technically it is the sum that is observed. However, only relative intensities are relevant, so the factor of $1/2$ can be ignored. Showing the average simplifies comparison to the individual object functions.)

is transferred to the specimen. This leads to an energy spectrum in the transmitted electrons that is characteristic of the energy levels of the specimen being studied. The high energy of the electron beam allows for excitation of a variety of processes, including core-level transitions in the atoms. These serve both to identify the elements in the sample, and allows one to quantify the amount present by use of a suitable reference standard.³⁴

Experimental Section

Sample Preparation. The CdSe nanocrystals were synthesized by standard methods,^{16,43} and “size focused” by the method of Peng et al.²⁰ with some modifications. Synthesis and workup were done under a nitrogen atmosphere inside a dri-box. The reaction solution consisted of a 2.5:1:84 by mass solution of dimethyl cadmium (Strem, vacuum distilled), selenium metal (shot, Strem, as received), and tributylphosphine (Strem, as received). A volume of 6 mL of the reaction solution was injected into 12 g of trioctylphosphine oxide (90%, Aldrich) maintained at 360 °C. As soon as the solution temperature dropped to 300 °C, an additional amount (0.5–4 mL, depending on the final size desired) of concentrated reaction solution (2.5:1:21 by mass) was added. The nanocrystals were then allowed to grow at 300 °C. Growth was monitored by taking absorption spectra of aliquots removed from the flask until the exciton peak ceased to narrow, at which point the reaction was stopped by removal of the heat source. The nanocrystals were isolated by precipitation from methanol and washed twice with methanol, ensuring complete removal of all starting materials. The dried powder was stored in the drybox.

The nanocrystals were wurtzite CdSe as verified by electron diffraction and high-resolution transmission electron microscopy (HRTEM). HRTEM images of the CdSe nanocrystals are shown in Figure 3 together with the solution phase absorption spectrum.

To mitigate contamination effects in the STEM due to the trioctylphosphine oxide (TOPO) surface ligand, the latter was exchanged with pyridine by heating the nanocrystals in anhydrous pyridine for several hours. The nanocrystals were subsequently precipitated with hexanes and dissolved in chloroform.

Poly(2-methoxy,5-(2'-ethyl-hexyloxy)-*p*-phenylenevinylene) (MEH-PPV) was prepared by the method of Wudl et al.⁴⁴ and dissolved in chloroform inside the drybox.

Methanol and chloroform were distilled from calcium hydride under ultrahigh purity (UHP) argon. Other solvents were distilled from sodium benzophenone under UHP argon.

STEM samples were prepared by mixing the MEH-PPV and CdSe solutions and spin-coating onto single-crystal NaCl substrates ({100} surfaces, Ted Pella Co.). Typical parameters were 20 μL of 2 mg mL^{-1} MEH-PPV/0.05 mg mL^{-1} CdSe solution, spun at 2000 rpm. The films were removed by dipping into a water surface, whereupon the film floats onto the surface as the NaCl dissolves away. The floating films were picked up with lacey carbon coated copper TEM grids (Ted Pella Co.). These processing conditions result in films of suitable thickness for STEM analysis with a significant fraction of isolated nanocrystals as well as some aggregates that aid in focusing at intermediate magnifications, while the lacey carbon assists focusing at low magnifications. The conductive nature of the polymer seems to prevent charging effects, especially when compared to Formvar substrates. At the same time contamination effects are less severe than for nanocrystals supported on a pure carbon film, possibly because the nanocrystals are fully encapsulated on all sides. At the same time, the lower density of the polymer relative to carbon reduces the background effects in the Z-STEM image, albeit at the cost of complicating the EELS analysis.

Specimens for EELS analysis were prepared in a glovebag (Aldrich Atmosbag) purged with dry nitrogen, however, the water bath was not degassed and may have been a source of oxygen. Samples were stored under nitrogen or argon. Specimens were loaded with a glovebag attached to the microscope under nitrogen flow (unfiltered, from a standard gas cylinder).

Samples for Z-contrast imaging were prepared in air, stored under argon, and loaded in air.

Film thicknesses were typically in the range from 150 to 200 Å as judged from the optical absorption of identical films spun onto glass slides (o.d. \approx 0.1 at the absorption peak of the polymer). Atomic force microscopy (AFM) measurements on similarly prepared films are consistent with these values but indicate deviations from planarity on the order of ± 25 Å, consistent with ellipsometry measurements.

Z-STEM. Atomic resolution Z-contrast imaging was performed in a VG microscopes model HB603U STEM operating at 300 kV with a nominal resolution of 1.3 Å. A Maximum entropy (MaxEnt)^{45–47} image reconstruction algorithm was used to remove noise from the image and deconvolute the resolution function due to the electron beam profile. The details are described elsewhere.³⁸ For visual presentation, image brightness and contrast was adjusted in NIH Image,⁴⁸ but intensities were measured on the unscaled images. Intensities were measured in NIH Image by manually selecting a region around each column to be analyzed. NIH Image then sums the pixel values in the selected region and determines the geometric center of the selected region. The latter is used as the coordinate for the column. The intensity values are corrected for the background intensity in the area surrounding the column.

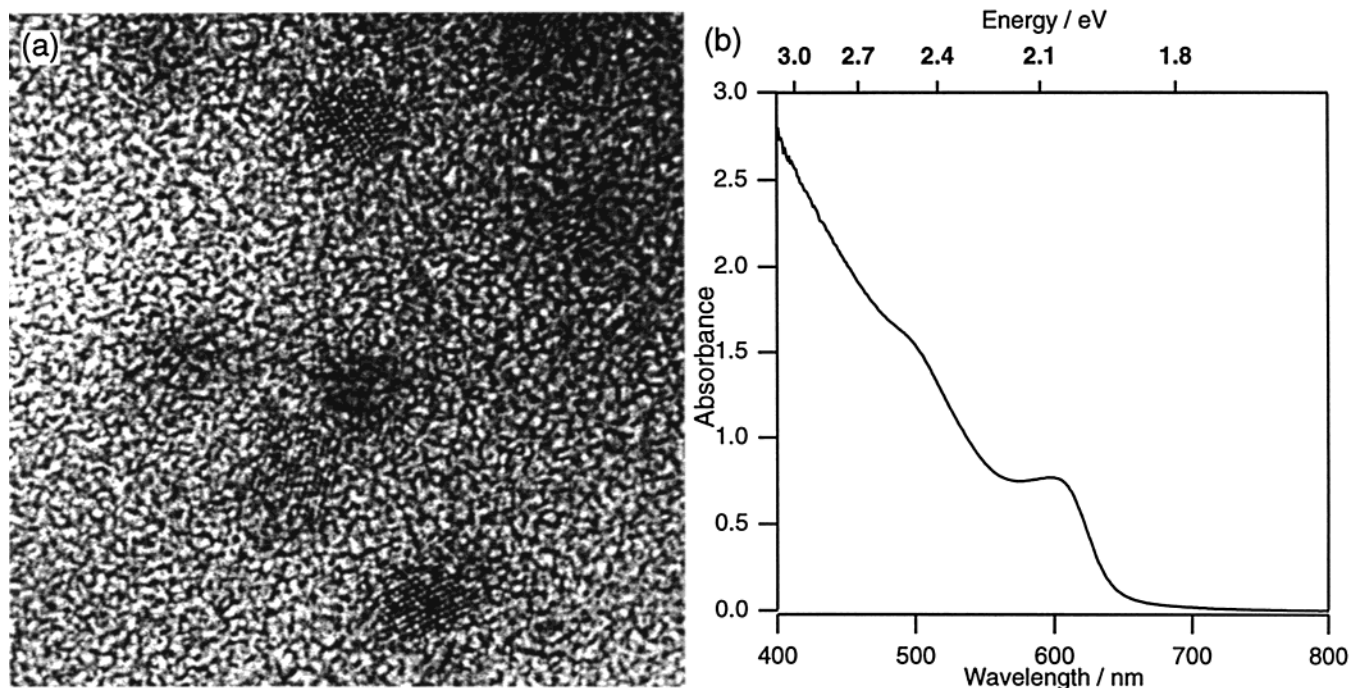


Figure 3. CdSe nanocrystals. (a) HRTEM of CdSe nanocrystals embedded in MEH-PPV polymer and (b) UV-vis absorption spectrum of same nanocrystals in chloroform solution (relative to a chloroform blank).

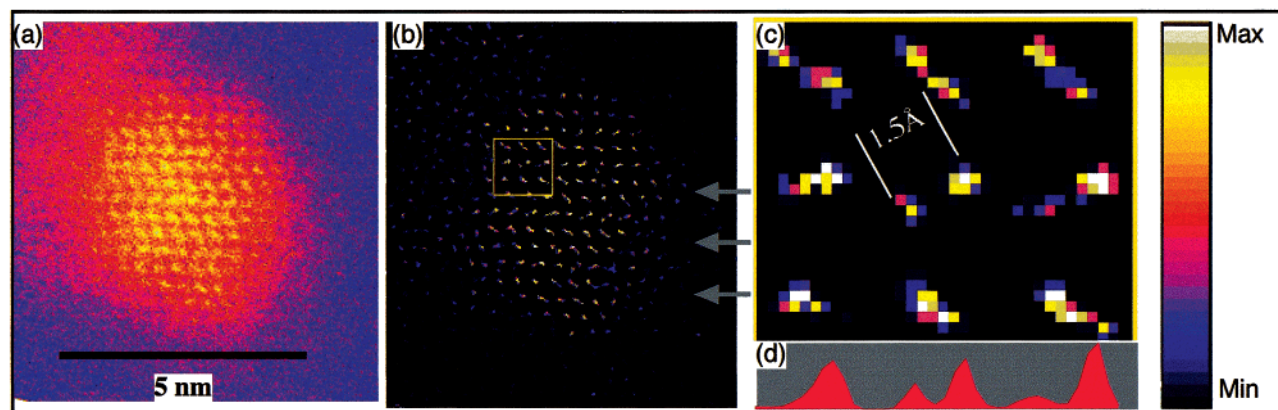


Figure 4. Z-STEM imaging. (a) Atomic Resolution Z-STEM Image of a 56 Å diameter (vertical axis) CdSe Nanocrystal using a false-color display. The color scale is shown to the right. A second nanocrystal is partially visible in the top left corner. The image has been aligned so that the [001] lattice vector is pointing up. (b) Maximum Entropy reconstruction of the nanocrystal object function for the image in (a). The arrows indicate stacking faults where the regular wurtzite (ABAB) stacking is interrupted by zinc blende stacking (ABCABC). The second nanocrystal is not on zone axis, hence the reconstruction results in spurious peaks, not aligned on a lattice. These peaks are ignored in the subsequent analysis. (c) Enlarged (7 \times) view of the area in (b) indicated by the square. The dumbbell pair in the center is clearly resolved showing the more strongly scattering Cd column to the top right, 1.5 Å away from the Se column. Other dumbbells can be resolved on account of the different scattering intensities, even if the intensity does not drop to zero between the columns. (d) Intensity profile for the middle row of dumbbell columns in (c). The two pairs on the right are resolved and the larger peaks correspond to the more intense Cd columns. The leftmost column pair is not resolved, but the intensity distribution matches the resolved columns.

EELS. EELS analysis was performed in a VG microscopes model HB501 STEM operating at 100 kV with an ultimate resolution of 2.2 Å. However, to improve the signal-to-noise ratio (SNR) for EELS data collection, the probe was run with low excitation of the condenser lens. The increased beam current comes at the expense of reduced spatial resolution. A parallel EELS system using a CCD detector with nearly single-electron sensitivity was employed. Spectra were corrected for the gain profile of the detector. The system is described in more detail in Duscher et al.⁴⁹ The energy dispersion was calibrated to the carbon K-edge absorption at 284 eV by acquiring spectra of the polymer substrate in a region without nanocrystals. The dispersion was typically adjusted to yield 1.5 eV per detector

channel. The energy uncertainty in each Channel is estimated at ± 0.3 eV (at 95% confidence).

EELS spectra were collected in the range from 500 to 950 eV. Data were analyzed using Wavemetrics Igor Pro⁵⁰. The preedge background for each EELS spectrum was fit to a power law function and subtracted from the data to obtain the Oxygen K-edge signal at 532 eV. Edge intensities were integrated in the range from 532 to 600 eV using Igor Pro's algorithm based on the trapezoidal method. To obtain the linescan shown in Figure 7, the probe was scanned immediately after acquiring the image.

To obtain EELS line profiles, an image was taken of the area of interest with a nanocrystal centered. The probe was then

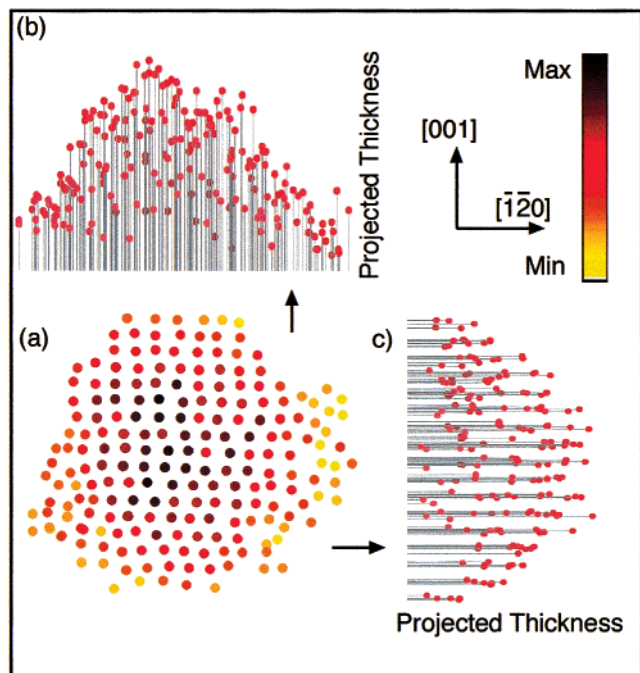


Figure 5. Intensity map of experimental image. (a) Intensity map measured from the MaxEnt reconstruction in Figure 4b. Each spot corresponds to a signal peak in the image, which may be a column, but can also arise from other sources (background noise, artifacts in the image reconstruction process, etc.). Where dumbbell columns were resolved, they were integrated together for this analysis. Darker spots correspond to more intense signals, as shown by the color scale in the top right section. Crystallographic directions are indicated by the arrows. (b) Thickness profile obtained by projecting the intensities in (a) along the horizontal $[120]$ direction. (Generically this is a $\langle 110 \rangle$ type direction. The conventional choice of $[100]$ for the zone axis label together with the hexagonal coordinate system produces this rather awkward index.) (c) Thickness profile obtained by projecting the intensities in (a) along the vertical $[001]$ direction.

scanned in a line along the x -direction across the center of the area of interest. Another image was taken after the linescan and scans with excessive image drift between the two images (more than ~ 10 Å) were rejected. EELS spectra were acquired successively at fixed signal integration times resulting in a series of EELS measurements at different segments along the scan line.

Results/Discussion

Z-STEM. The Z-STEM image of a nanocrystal near $[100]$ zone axis orientation is shown in Figure 4. Part a shows the raw data, and part b is the MaxEnt reconstruction of the object function with the point spread function of the microscope removed. Three $\langle 001 \rangle$ stacking faults traverse the nanocrystal as indicated by the arrows. These faults correspond to polymorphism in bulk wurtzite crystals and are common with this type of nanocrystal.^{16,32,51}

Part c shows a magnified view of the area in part b indicated by the square. The dumbbell pairs of Cd and Se columns spaced 1.5 Å apart are just resolved. The different intensities indicate that the Cd comprises the top right column of the dumbbell pair. On the basis of the contrast in the atomic columns, the $[001]$ lattice vector direction is assigned as up in the image.

Not all columns are as well resolved within this image. This could indicate strain in the lattice or beam-broadening from the polymer matrix, but it could also be due to image noise. The maximum signal-to-noise ratio (SNR) in the raw image is approximately 2. While the atomic centers are well separated

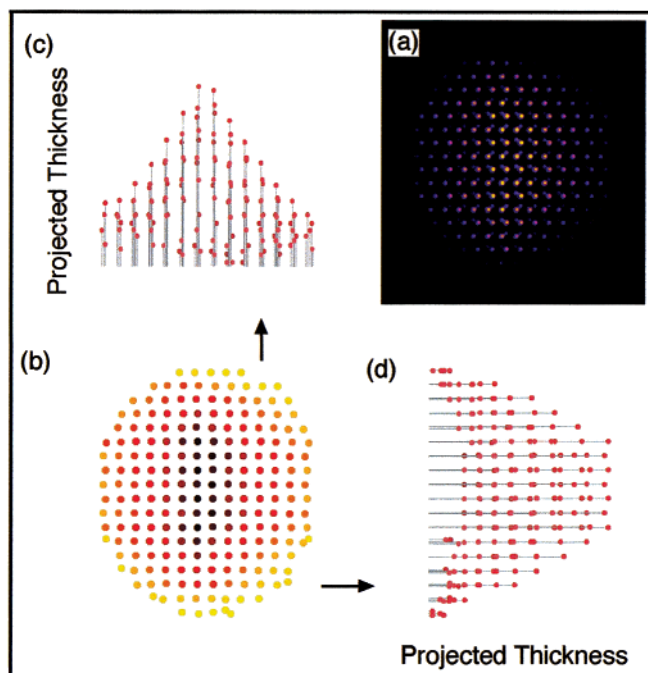


Figure 6. Image simulation. (a) Calculated image of a 56 Å diameter (vertical axis) nanocrystal in $[100]$ zone axis orientation with the $[001]$ vector pointing up in the image, based on the model of Shiang et al.³² The color scale is the same as in Figure 4. (b) Intensity map of the image in (a). Color scale is the same as the intensity map in Figure 5. (c) Thickness profile obtained by integrating and projecting the intensities in (b) along the horizontal direction. (d) Thickness profile obtained by integrating and projecting the intensities in (b) along the vertical direction.

(1.5 Å), the 1s Bloch states have diameters on the order of 0.8 Å, so some overlap between the Se and Cd states may be expected. The low SNR then makes it very difficult to accurately resolve the dumbbells. However, 14 dumbbells are resolvable and they all support the assignment of the $[001]$ direction.

It is assumed that the Cd and Se columns are of equal thickness within each dumbbell column. One may reasonably expect them to differ by one atom at the entrance and exit surfaces each, depending on the exact nature of the surface termination. For the nanocrystal shown the thickness should be on the order of 15–18 atoms so the maximum error would be 13% which cannot account for the contrast difference observed. Hence the assignment of the elemental identities is clear-cut! Using this assignment we thus identify the top surface as the Cd-terminated (001) surface and its counterpart on the bottom as the Se-terminated (00 $\bar{1}$). Further improvements in resolving the atomic structures of these surfaces might help elucidate whether these surfaces cause the dipole moment reported for these types of nanocrystals.^{52–54}

Integrating the total intensity of each (compositionally invariant) dumbbell pair one obtains the spatially resolved thickness map in Figure 5a. Projecting the thickness map along the two axes in the image results in the thickness envelopes depicted in parts b and c of Figure 5. The thickness envelope corresponds to the expected shape based on previous HRTEM studies³² on such nanocrystals.

For comparison, we have calculated a Z-STEM image for a 56 Å diameter nanocrystal based on the model of Shiang et al.³² The model was built in Crystallmaker 4.0⁵⁵ using reference data for CdSe.⁵⁶ The model data was imported into IDL 5.3⁵⁷ and the scattering intensities were calculated for each column position according to eq 2. The intensities were then mapped

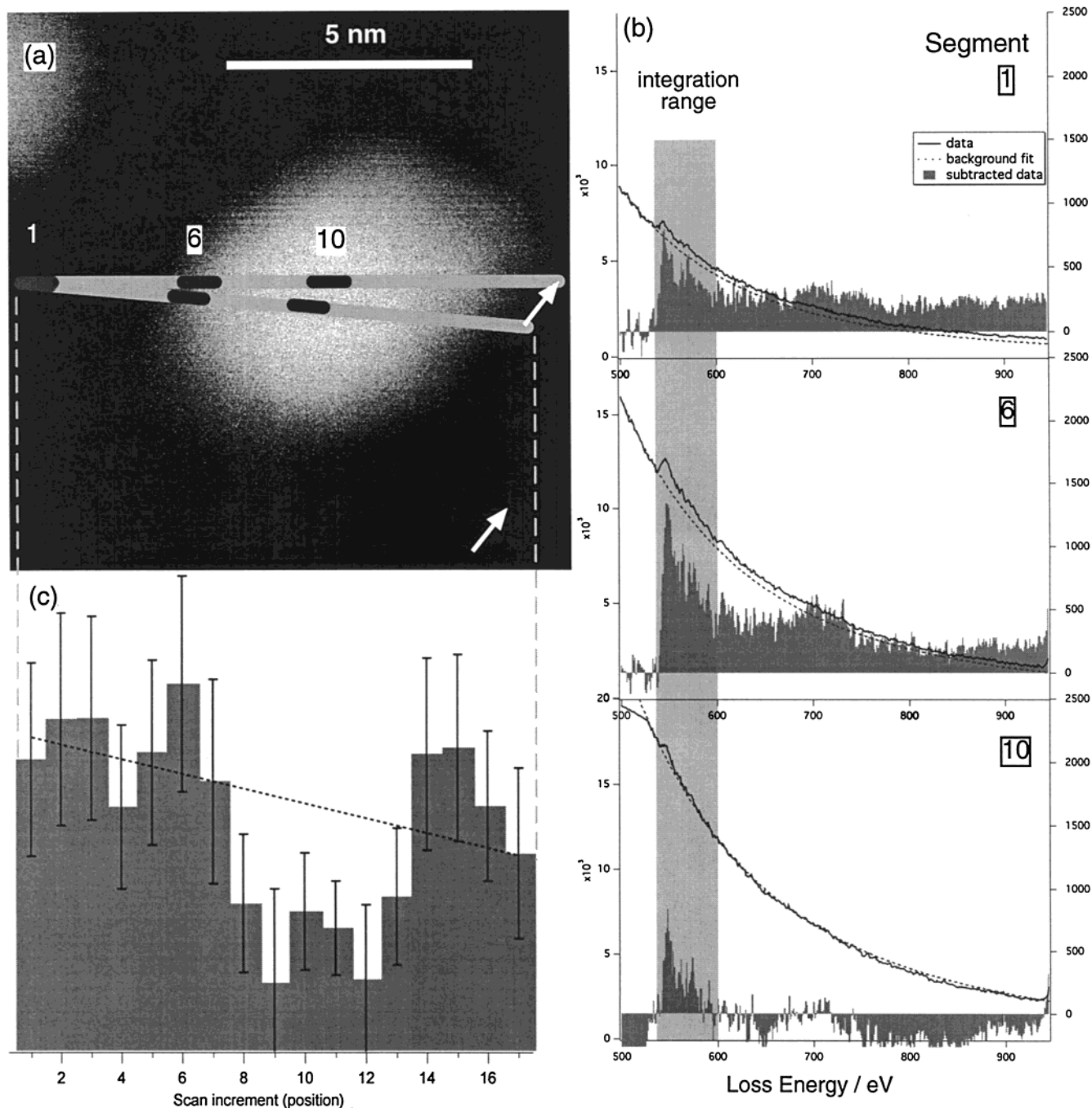


Figure 7. EELS analysis of single nanocrystal. (a) Z-STEM image of a single nanocrystal taken before scanning the EELS spectrum. Atomic columns are not resolved. The horizontal line indicates the path taken by the scanning probe in acquiring EELS spectra. The numbered segments correspond to sampling intervals. The total drift during acquisition is approximately 9 Å, determined by imaging immediately before and after the EELS acquisition. The magnitude and direction of the drift are indicated by the arrow in the lower right corner. Assuming the drift is linear during the entire acquisition the nominal scan line is corrected by subtracting the drift vector, resulting in the angled scan line shown. (b) EELS spectra at various points across the line in (a). Numbers correspond to the segment labels in (a). The raw spectra (solid lines) are shown together with the background fits (dotted lines) on a common scale (left, in units of detector counts). The background subtracted EELS edges (gray histograms) are shown on a separate scale (right, counts). The scales are the same for each of the spectra. The gray rectangle indicates the range of energies integrated to obtain the edge intensity used for the histogram in part (c). The discontinuity at low energy in segment 10 is due to saturation of the CCD detector and is not included in the fit. (c) Intensity profile of the oxygen K-edge signal, based on integrating the EELS spectra for each line segment. Each bar corresponds to a scan segment in (a). The error bars indicate the 95% confidence limits in the measurement based on the uncertainty in the energy scale and the standard deviation of the residuals obtained from the background fit. The dashed line indicates a linear least-squares fit to the segments that are not on the nanocrystal (1–5 and 17) and can be taken as an estimate of the oxygen background level arising from the polymer substrate.

to a 5 pixels/Å grid, which is close to the resolution in the experimental image. The result was convoluted with a 0.8 Å (4 pixels) FWHM 2D Gaussian to simulate the spatial extent of the 1s states. The calculated image is displayed in Figure 6 (a) and was analyzed in NIH Image. Column positions and

intensities were measured automatically using threshold discrimination. The corresponding intensity map and thickness profiles are displayed in parts b– d.

Notable features of the calculated image are the clear shape profile and discrete column positions. This agrees well with the

experimental image although the correspondence is worse for the [001] projection. This is due to the stacking faults traversing the nanocrystal. Each fault shifts the crystal lattice by $1/3$ lattice spacing horizontally. This misaligns the atomic columns when projected along [001] and distorts the shape profile. In comparison, there is no corresponding misalignment when projecting along $[\bar{1} 20]$ as the faults are parallel to this direction. Some of the disagreement also stems from spurious intensity peaks in the background region which confuse the analysis. This also makes it very difficult to distinguish the nanocrystal surface. The spurious peaks arise because the MaxEnt algorithm tends to overfit smooth image areas. Alternate image reconstruction algorithms^{58,59} avoid this overfitting, and we are in the process of adapting them to Z-STEM imaging.

Another noteworthy observation concerns the quantization of the column intensities in the calculated image. While there are discrete intensity ranges observable in the projections, the quantization is not perfect. Rather there are small variations from column to column. This arises from the limited sampling of the 1s states on our grid coupled with the finite dynamic range. The unconvoluted intensity map shows perfect quantization (by definition since it is based on eq 2). This implies that for a fixed size sampling grid with a finite dynamic range (such as the detection system on our STEM) the sensitivity to thickness variations depends on the magnification. The same is true for the column positions, which show some scatter about the lattice positions.

The astute observer will also notice that there are columns in the intensity map where none are visible in the model image. The display image has less dynamic range (8-bit) than the model calculation which was matched to the 12-bit dynamic range of our detection system. Suitable scaling of the image contrast/brightness will reveal these features to the human observer and they are of course amenable to computer analysis. Nonetheless, the dynamic range affects the detection limits. With the 12-bit dynamic range, columns containing two or fewer Se atoms are below the detection limit under ideal conditions, whereas single Cd atoms can be detected. In practice the detection limits are probably higher due to image noise. Either way, the possibility of "invisible" columns must be taken into account when analyzing image data for the thinnest portions of the nanocrystal.

Finally, it must be pointed out that while the model presented here fits the data, this does not rule out other models that may fit equally well. The main problem in unambiguously reconstructing the image is the low SNR, resulting in fairly large uncertainties in reconstructed intensities. While increasing signal acquisition times will immediately improve the SNR, it was not feasible within the conditions of the present experiment. This is due to specimen drift and beam damage of the substrate (which is probably in part responsible for the drift). Presently, beam damage is the limiting factor as the MEH-PPV seems to degrade under the electron beam and cause contamination buildup. We are currently testing an alternate polymer system for use as a matrix. A pure carbon film substrate would of course be ideal, but adhesion of the nanocrystals to the film generally requires ligands which cause contamination under the beam. It may be possible to deposit pyridine-coated nanocrystals onto thin carbon substrates and then remove the pyridine by heating inside a vacuum chamber followed by evaporation of a carbon overcoat to protect the nanocrystals from oxidation and keep them fixed onto the film. The drawback to this approach is that the higher density of carbon will result in additional beam spreading and additional background scatter, further degrading the image quality.

It must also be pointed out that simply increasing acquisition time has a diminishing rate of return as a doubling of the SNR requires quadrupling the acquisition time. Eventually throughput becomes a factor. Consequently improved instrumentation is desirable. This point is further addressed in the future work section.

EELS. An EELS linescan across a different CdSe nanocrystal is presented in Figure 7. Spectra in the vicinity of the oxygen K-edge were collected in seventeen 4s increments while continuously scanning the probe along the line indicated in part a. The total drift in the image for the entire linescan was about 9–10 Å, as indicated by the arrow in the figure. Raw spectra are shown in part b together with the background-subtracted oxygen K-edges.

The increase in the background signal level as the scan traverses the nanocrystal is due to the Cd M-edge loss at 404 eV. The rather diffuse nature of M-edges makes it difficult to use this for quantitation. It does, however, serve to verify both the chemical identity of the particle being investigated, as well as its thickness at each scan segment and thus gives an indication of position on the particle.

The integrated edge intensities in Figure 7c indicate the relative oxygen content as a function of position along the scan. The dashed line indicates a fit to the signal in the substrate-only region of the scan and can be taken as the background level due to the polymer matrix. As the scan traverses the nanocrystal, the oxygen signal drops below this level due to the volume of polymer being excluded by the nanocrystal. There appears to be a slight increase of the oxygen signal at the edges of the nanocrystal, but this increase is just within the error limits of the measurement. Hence while the increase is suggestive of an oxide shell, the quality of the data is insufficient to prove this conclusively at the 95% confidence level. Improving this requires better signal-to-noise statistics than are available with the present setup. To improve this we are investigating more stable substrates (which will allow longer signal integration) as well as upgrading the electron beam brightness.

Taking the film thickness based on optical absorption to be ~15 nm and assuming a density for the polymer film (~1.5 g/cm³ based on the buoyancy of gelled polymer in chloroform) allows estimation of the amount of material being interrogated in each scan segment. On the basis of the empirical formula for MEH-PPV (C₁₇H₂₄O₂), our acquisition parameters correspond to detecting less than 10 atoms of oxygen within a scan increment on the polymer substrate and less than 5 atoms at the center of the nanocrystal. The slight rise at the nanocrystal edge would be 1–2 atoms of oxygen at this scale. This is of course a rather crude estimate. It also ignores local variations in the film thickness. The latter probably give rise to the sloping background signal indicated in Figure 7c. For accurate quantitation a better calibration standard is required. However, it provides an approximate indication of the sensitivity to minute quantities of oxygen.

The EELS linescans would be easier to interpret if the polymer matrix did not contribute to the oxygen signal. To that end we are currently testing the use of poly-3-hexylthiophene (P3HT) as the polymer matrix. Any oxygen then detected could be unambiguously assigned to the nanocrystals. This improves the qualitative analysis but does not help with quantitation, which requires some way to calibrate the signal intensity.

Inorganic oxide nanocrystals^{60–63} that can be co-dispersed with the nanocrystals of interest might serve as a quantification standard. Since the EELS provides the requisite qualitative analysis, these would not be confused with the particles of

interest and the imaging abilities of the STEM could give an accurate size measurement. If the composition is known, this then provides a useful reference signal.

We should also point out that scans at lower energy exhibit no indication of the nitrogen K-edge at 400 eV, which corroborates other observations^{64,65} that the pyridine ligand is removed from the nanocrystals during processing into the thin film specimen. Thus, barring any contaminants at the surface, the nanocrystals are in intimate contact with the polymer as is desirable for applications involving charge transfer between the polymer matrix and nanocrystals (e.g., LED's^{13,66} and photo-voltaics^{11,64,67,68}).

Conclusions

Z-contrast STEM is capable of resolving the lattice polarity in CdSe nanocrystals and thus can be used to uniquely identify different surfaces on a nanocrystal. Z-contrast STEM can also provide thickness information directly from the image. By comparing intensities from compositionally similar columns, a map of relative thickness across a nanocrystal is obtained that matches the predicted shape to within the error of the measurement. Reducing the amount of error requires improvement in the image SNR.

STEM-EELS can provide qualitative elemental information on sub-nanometer length scales and thus can be used to analyze nanocrystal surfaces. Quantitation is limited by (1) need for a good reference standard and (2) counting statistics.

Future Work

The main limitations in both Z-STEM and EELS are the weak signals obtained and thus the low SNR. With the advent of spherical aberration correctors,⁶⁹ Z-contrast images will show much greater contrast and higher SNR which will make techniques such as discussed here very much more sensitive. In addition it is possible to detect optical emission (cathodoluminescence) from nanocrystals^{70–72} excited by the electron beam allowing the possibility to compare the optical properties of nanocrystals to their three-dimensional shape and surface termination.

Acknowledgment. The research presented here was funded by the Department of Energy, Basic Energy Sciences, Materials Sciences Division Contract DE-AC05-84OR21400 and the National Renewable Energy Laboratory, Subcontract AAD-9-18668-11. We thank G.E. Jellison and C. Chen for ellipsometry measurements on MEH-PPV films. We also thank the Hanusa group at Vanderbilt University for use of the Crystallmaker software. A.V.K. gratefully acknowledges the assistance of P.D. Nellist, B.E. Rafferty, G. Duscher, and M. F. Chisholm in learning the operation of the STEMs.

References and Notes

- Mahtab, R.; Harden, H. H.; Murphy, C. J. *J. Am. Chem. Soc.* **2000**, *122*, 14.
- Lakowicz, J. R.; Gryczynski, I.; Gryczynski, Z.; Murphy, C. J. *J. Phys. Chem. B* **1999**, *103*, 7613.
- Bruchez, M.; Moronne, M.; Gin, P.; Weiss, S.; Alivisatos, A. P. *Science* **1998**, *281*, 2013.
- Chan, W. C. W.; Nie, S. M. *Science* **1998**, *281*, 2016.
- Nanda, J.; Sapra, S.; Sarma, D. D.; Chandrasekharan, N.; Hodes, G. *Chem. of Mater.* **2000**, *12*, 1018.
- Kho, R.; Nguyen, L.; Torres-Martinez, C. L.; Mehra, R. K. *Biochem. Biophys. Res. Commun.* **2000**, *272*, 29.
- Henglein, A. *Pure Appl. Chem.* **1984**, *56*, 1215.
- Henglein, A. *Ber. Bunsen-Ges. Phys. Chem. Chem. Phys.* **1997**, *101*, 1562.
- Gao, M. Y.; Lesser, C.; Kirstein, S.; Mohwald, H.; Rogach, A. L.; Weller, H. *J. Appl. Phys.* **2000**, *87*, 2297.
- Vlasov, Y. A.; Nan, Y.; Norris, D. J. *Adv. Mater.* **1999**, *11*, 165.
- Huynh, W. U.; Xiaogang, P.; Alivisatos, A. P. *Adv. Mater.* **1999**, *11*, 923.
- Konenkamp, R.; Hoyer, P.; Wahi, A. *J. Appl. Phys.* **1996**, *79*, 7029.
- Colvin, V. L.; Schlamp, M. C.; Alivisatos, A. P. *Nature* **1994**, *370*, 354.
- Greenham, N. C.; Xiaogang, P.; Alivisatos, A. P. A CdSe nanocrystal/MEH-PPV polymer composite photovoltaic. Presented at the First NREL Conference, Denver, CO, 1997.
- Klein, D. L.; Roth, R.; Lim, A. K. L.; Alivisatos, A. P.; McEuen, P. L. *Nature* **1997**, *389*, 699.
- Murray, C. B.; Norris, D. J.; Bawendi, M. G. *J. Am. Chem. Soc.* **1993**, *115*, 8706.
- Goldstein, A. N.; Echer, C. M.; Alivisatos, A. P. *Science* **1992**, *256*, 1425.
- Vossmeier, T.; Reck, G.; Katsikas, L.; Haupt, E. T. K.; Schulz, B.; Weller, H. *Science* **1995**, *267*, 1476.
- Herron, N.; Calabrese, J. C.; Farneth, W. E.; Wang, Y. *Science* **1993**, *259*, 1426.
- Peng, X. G.; Wickham, J.; Alivisatos, A. P. *J. Am. Chem. Soc.* **1998**, *120*, 5343.
- Klein, D. L.; McEuen, P. L.; Bowen Katari, J. E.; Roth, R.; Alivisatos, A. P. *Appl. Phys. Lett.* **1996**, *68*, 2574.
- Banin, U.; Cao, Y.; Katz, D.; Millo, O. *Nature* **1999**, *400*, 542.
- Efros, A. L.; Rosen, M. *Phys. Rev. Lett.* **1997**, *78*, 1110.
- Nirmal, M.; Dabbousi, B. O.; Bawendi, M. G.; Macklin, J. J.; Trautman, J. K.; Harris, T. D.; Brus, L. E. *Nature* **1996**, *383*, 802.
- Blanton, S. A.; Hines, M. A.; Guyot-Sionnest, P. *Appl. Phys. Lett.* **1996**, *69*, 3905.
- Tittel, J.; Gohde, W.; Koberling, F.; Basche, T.; Kornowski, A.; Weller, H.; Eychmuller, A. *J. Phys. Chem. B* **1997**, *101*, 3013.
- Dahan, M.; Laurence, T.; Schumacher, A.; Chemla, D. S.; Alivisatos, A. P.; Sauer, M.; Weiss, S. *Biophys. J.* **2000**, *78*, 2270.
- Empedocles, S.; Bawendi, M. *Acc. Chem. Res.* **1999**, *32*, 889.
- Pokrant, S.; Whaley, K. B. *Eur. Phys. J. D* **1999**, *6*, 255.
- Leung, K.; Pokrant, S.; Whaley, K. B. *Phys. Rev. B-Condens. Matter* **1998**, *57*, 12291.
- Hill, N. A.; Whaley, K. B. *J. Chem. Phys.* **1994**, *100*, 2831.
- Shiang, J. J.; Kadavanich, A. V.; Grubbs, R. K.; Alivisatos, A. P. *J. Phys. Chem.* **1995**, *99*, 17417.
- Kadavanich, A. V.; Mews, A.; Tolbert, S. H.; Peng, X.; Schlamp, M. C.; Lee, J. C.; Alivisatos, A. P. *Adv. Microcryst. Nanocryst. Semicond. - 1996, Symp.* **1996**.
- Williams, D. B.; Carter, C. B. *Transmission Electron Microscopy: A Textbook for Materials Science*; Plenum Press: New York, 1996.
- Kisielowski, C.; Schwander, P.; Baumann, F. H.; Seibt, M.; Kim, Y.; Ourmazd, A. *Ultramicroscopy* **1995**, *58*, 131.
- Ourmazd, A.; Baumann, F. H.; Bode, M.; Kim, Y. *Ultramicroscopy* **1990**, *34*, 237.
- Schwander, P.; Rau, W. D.; Ourmazd, A. *J. Microsc. (Oxford)* **1998**, *190*, 171.
- Nellist, P. D.; Pennycook, S. J. *Ultramicroscopy* **1999**, 111.
- Pennycook, S. J.; Nellist, P. D. Z-Contrast Scanning Transmission Electron Microscopy. In *Impact of Electron Scanning Probe Microscopy on Materials Research*; Rickerby, D., Valdrè, G., Valdrè, U., Eds.; Kluwer Academic Publishers: The Netherlands, 1999.
- Pennycook, S. J.; Jesson, D. E. *Phys. Rev. Lett.* **1990**, *64*, 938.
- Jesson, D. E.; Pennycook, S. J. *Proc. R. Soc. London, Ser. A (Math. Phys. Sci.)* **1993**, *441*, 261.
- Nellist, P. D.; Pennycook, S. J. *Science* **1996**, *274*, 413.
- Bowen Katari, J. E.; Colvin, V. L.; Alivisatos, A. P. *J. Phys. Chem.* **1994**, *98*, 4109.
- Wudl, F.; Srdanov, G. Conducting Polymer formed of Poly(2-Methoxy, 5-(2'-Ethyl-Hexyloxy)-p-Phenylenevinylene). In *United States Patent*; Patent and Trademark Office: Washington, DC, 1993; Vol.: The Regents Of The University of California, Oakland, California.
- Burch, S. F.; Gull, S. F.; Skilling, J. *Computer Vision, Graphics, and Image Processing* **1983**, *23*, 113.
- Skilling, J.; Bryan, R. K. *Monthly Notices of the Royal Astronomical Society* **1984**, *211*, 111.
- Skilling, J.; Sibisi, S. Fundamentals of MAXENT in data analysis; Invited and Contributed Papers from the Conference, Chilton, UK, 1990
- Rasband, W. NIH Image; Version 1.62; National Institutes of Health: Bethesda, MD (<http://rsb.info.nih.gov/nih-image/>).
- Duscher, G.; Browning, N. D.; Pennycook, S. J. *Phys. Status Solidi A* **1998**, *166*, 327.
- Igor Pro, Version 3.16 (PPC); Wavemetrics Inc.: Lake Oswego, OR, 2000 (<http://www.wavemetrics.com/>).
- Peng, X. G.; Schlamp, M. C.; Kadavanich, A. V.; Alivisatos, A. P. *J. Am. Chem. Soc.* **1997**, *119*, 7019.
- Shim, M.; Guyot-Sionnest, P. *J. Chem. Phys.* **1999**, *111*, 6955.

- (53) Schmidt, M. E.; Blanton, S. A.; Hines, M. A.; Guyot-Sionnest, P. *J. Chem. Phys.* **1997**, *106*, 5254.
- (54) Blanton, S. A.; Leheny, R. L.; Hines, M. A.; Guyot-Sionnest, P. *Phys. Rev. Lett.* **1997**, *79*, 865.
- (55) Palmer, D. C. Crystallmaker, Version 4.0.6 PowerPC; Crystallmaker Software: Bicester, Oxfordshire, OX6 7BS, UK, 2000 (<http://www.crystallmaker.com/>)
- (56) JCPDS-ICDD, Powder Diffraction File 08-0459, CdSe, hexagonal. International Centre for Diffraction Data: Newtown Square, PA, 1996 (<http://www.icdd.com/>).
- (57) IDL, Version. 5.3; Research Software, Inc.: Boulder, CO, 1999 (<http://www.rsinc.com>).
- (58) Pina, R. K.; Puetter, R. C. *Publ. Astron. Soc. Pac.* **1993**, *105*, 630.
- (59) Dixon, D. D.; Johnson, W. N.; Kurfess, J. D.; Pina, R. K.; Puetter, R. C.; Purcell, W. R.; Tumer, T. O.; Wheaton, W. A.; Zych, A. D. *Astron. Astrophys. Suppl. Ser.* **1996**, *120*, C683.
- (60) Rockenberger, J.; Scher, E. C.; Alivisatos, A. P. *J. Am. Chem. Soc.* **1999**, *121*, 11595.
- (61) Rockenberger, J.; zum Felde, U.; Tischer, M.; Troger, L.; Haase, M.; Weller, H. *J. Chem. Phys.* **2000**, *112*, 4296.
- (62) Hoyer, P.; Weller, H. *Chem. Phys. Lett.* **1994**, *221*, 379.
- (63) Kan, S. H.; Yu, S.; Peng, X. G.; Zhang, X. T.; Li, D. M.; Xiao, L. Z.; Zou, G. T.; Li, T. J. *J. Colloid Interface Sci.* **1996**, *178*, 673.
- (64) Greenham, N. C.; Xiaogang, P.; Alivisatos, A. P. *Phys. Rev. B (Condens. Matter)* **1996**, *54*, 17628.
- (65) Kim, B. S.; Avila, L.; Brus, L. E.; Herman, I. P. *Appl. Phys. Lett.* **2000**, *76*, 3715.
- (66) Schlamp, M. C.; Peng, X.; Alivisatos, A. P. *J. Appl. Phys.* **1997**, *82*, 5837.
- (67) Ginger, D. S.; Greenham, N. C. *Synth. Met.* **1999**, *101*, 425.
- (68) Ginger, D. S.; Greenham, N. C. *Phys. Rev. B (Condens. Matter)* **1999**, *59*, 10622.
- (69) Krivanek, O. L.; Dellby, N.; Lupini, A. R. *Ultramicroscopy* **1999**, *78*, 1.
- (70) Fafard, S.; Leon, R.; Leonard, D.; Merz, J. L.; Petroff, P. M. *Superlattices Microstruct.* **1994**, *16*, 303.
- (71) Leon, R.; Petroff, P. M.; Leonard, D.; Fafard, S. *Science* **1995**, *267*, 1966.
- (72) Rodriguez-Viejo, J.; Jensen, K. F.; Mattoussi, H.; Michel, J.; Dabbousi, B. O.; Bawendi, M. G. *Appl. Phys. Lett.* **1997**, *70*, 2132.